First Census of Gas-phase Metallicity Gradients of Star-forming Galaxies in Overdense Environments at Cosmic Noon

Zihao Li[1] [iD], Xin Wang[2] [iD], Zheng Cai[1] [iD], Dong Dong Shi[3] [iD], Xiaohui Fan[4] [iD], Xian Zhong Zheng[3] [iD], Matthew A. Malkan[5] [iD],
Harry I. Teplitz[2] [iD], Alaina L. Henry[6] [iD], Fuyan Bian[7] [iD], and James Colbert[2] [iD]

[1] Department of Astronomy, Tsinghua University, Beijing 100084, People's Republic of China; zcai@mail.tsinghua.edu.cn
[2] Infrared Processing and Analysis Center, Caltech, 1200 E. California Boulevard, Pasadena, CA 91125, USA
[3] Purple Mountain Observatory, Chinese Academy of Sciences, 10 Yuan Hua Road, Nanjing 210023, People's Republic of China
[4] Steward Observatory, University of Arizona, 933 North Cherry Avenue, Tucson, AZ 85721, USA
[5] Department of Physics and Astronomy, University of California, Los Angeles, CA 90095-1547, USA
[6] Space Telescope Science Institute, 3700 San Martin Drive, Baltimore, MD, 21218, USA
[7] European Southern Observatory, Alonso de Córdova 3107, Casilla 19001, Vitacura, Santiago 19, Chile

Abstract

We report the first spatially resolved measurements of gas-phase metallicity radial gradients in star-forming galaxies in overdense environments at $z \gtrsim 2$. The spectroscopic data are acquired by the MAMMOTH-Grism survey, a Hubble Space Telescope (HST) cycle 28 medium program. This program is obtaining 45 orbits of WFC3/IR grism spectroscopy in the density peak regions of three massive galaxy protoclusters (BOSS 1244, BOSS 1542, and BOSS 1441) at $z = 2$–3. Our sample in the BOSS 1244 field consists of 20 galaxies with stellar mass ranging from $10^{9.0}$ to $10^{10.3} M_\odot$, star formation rate (SFR) from 10 to 240 $M_\odot$ yr^{-1}, and global gas-phase metallicity ($12 + \log(O/H)$) from 8.2 to 8.6. At 1σ confidence level, 2/20 galaxies in our sample show positive (inverted) gradients—the relative abundance of oxygen increasing with galactocentric radius, opposite the usual trend. Furthermore, 1/20 shows negative gradients, and 17/20 are consistent with flat gradients. This high fraction of flat/inverted gradients is uncommon in simulations and previous observations conducted in blank fields at similar redshifts. To understand this, we investigate the correlations among various observed properties of our sample galaxies. We find an anticorrelation between metallicity gradient and global metallicity of our galaxies residing in extreme overdensities, and a marked deficiency of metallicity in our massive galaxies as compared to their coeval field counterparts. We conclude that the cold-mode gas accretion plays an active role in shaping the chemical evolution of galaxies in the protocluster environments, diluting their central chemical abundance, and flattening/inverting their metallicity gradients.

1. Introduction

Metallicity gradients can be a diagnostic of several evolutionary processes in galaxies, including gas inflows and outflows, star formation and evolution (Finlator & Davé 2008; Peng & Maiolino 2014), and mergers (Rupke et al. 2010). Radial metallicity gradients have been under study for decades (Searle 1971; Pagel & Edmunds 1981; Hou et al. 2000). Growing interest in this field has prompted more observations in recent years (Swinbank et al. 2012; Jones et al. 2013; Leethochawalit et al. 2016; Förster Schreiber et al. 2018), together with numerical simulations (Ma et al. 2017; Tissera et al. 2019; Hemler et al. 2021). The normal trend of gas-phase metallicity decreases from the inside out, the gradient of which is negative, and we call it inverted if the gradient is positive in the opposite case. Some previous works show negative gradients in local field galaxies (Ho et al. 2015) as well as at higher redshift (Wang et al. 2017, hereafter W17), and positive (inverted) gradients are also found at both local, intermediate ($0.1 \lesssim z \lesssim 0.8$) (Carton et al. 2018), and higher redshift up to $z \sim 3$ (Cresci et al. 2010; Wang et al. 2019). The meaning of the different gradient behaviors is still under debate—more observations, as well as simulations, are still needed.

A plausible explanation for inverted gradients is "cold-mode" gas accretion, which has long been recognized to play a crucial role in feeding baryonic gas to galaxies (Kereš et al. 2005; Dekel et al. 2009). The cold-mode accretion dominates low-mass galaxies (with stellar mass $M_* \lesssim 10^{10.3} M_\odot$), where gas from cold dense intergalactic filaments gains gravitational energy and flows into the galaxies at lower temperatures ($T < 10^5$ K), instead of being shock-heated to the virial temperature of the dark matter (DM) halo ($T \sim 10^6$ K for an $M_h \sim 10^{12} M_\odot$ halo) before cooling and forming stars (Dekel & Birnboim 2006). The latter is conventionally referred to as "hot-mode" accretion, which dominates high-mass galaxies. In the cold-mode accretion scenario, the primordial gas directly flows into the center of galaxies and dilutes the metallicity of the central gas, which disturbs the original distribution of chemical abundance and thus flattens or even inverts the metallicity gradients. The transition between cold and hot mode happens at stellar mass $M_* \sim 10^{10.3} M_\odot$ or in terms of halo mass $M_h \sim 10^{11.4} M_\odot$ (Kereš et al. 2005). However, for galaxies at redshift $z \gtrsim 2$, cold-mode accretion could still exist in massive galaxies $M_* \gtrsim 10^{10.3} M_\odot$ (Dekel et al. 2009). At high redshift, the cold gas fed by dark matter filaments can penetrate deep into galaxies with halos more massive than the

shock-heating scale, where the gas along filaments cools before the pressure develops to support a shock.

The main observational challenge is that sub-kiloparsec (sub-kpc) resolution (angular resolution $\lesssim 0''\!.2$ at $z \sim 2$) is required to accurately measure spatial distributions of metallicity in galaxies. Building such a sample for high-z galaxies often suffers from the relatively poor spatial resolution of seeing-limited data, which fails to resolve the inner structures of distant galaxies (Carton et al. 2018; Curti et al. 2020). On the other hand, Förster Schreiber et al. (2018, hereafter F18) built a sub-kpc-resolution galaxy sample at $z \sim 2$ using SINFONI at the ESO Very Large Telescope (VLT), assisted with adaptive optics. Wang et al. (2020, hereafter W20) present the first large sub-kpc-resolution sample via grism spectroscopy from the Hubble Space Telescope (HST) in the redshift range of $1.2 \lesssim z \lesssim 2.3$. Simons et al. (2021) further extend such analyses to a wider redshift range of $0.6 \lesssim z \lesssim 2.6$.

In this work, we obtain the first measurements of radial metallicity gradients of galaxies in overdense environments at $z \gtrsim 2$ using the data acquired by the MAMMOTH-Grism slitless spectroscopic survey. This survey is a medium program in Hubble Space Telescope cycle 28 (GO-16276, P.I. Wang), allocated a total of 45 orbits of WFC3/G141 grism spectroscopy and WFC3/F125W pre-imaging in the central field of three of the most massive galaxy protoclusters at cosmic noon. This paper only includes galaxies in the BOSS 1244 protocluster.

This paper is organized as follows. In Section 2, we describe the grism data reduction, sample selection, and metallicity measurement method. We present our findings on the relation between galaxy mass and metallicity gradient in Section 3. Our conclusions are given in Section 4. In this paper, we adopt the AB magnitude system and assume a flat ΛCDM cosmology with $\Omega_m = 0.3$, $\Omega_\Lambda = 0.7$, and $H_0 = 70$ km s^{-1} Mpc^{-1}. The metallic lines are indicated in the following manner for brevity, [O III] $\lambda 5008 := $ [O III], [O II]$\lambda\lambda 3727,3730 := $ [O II], [Ne III] $3869 := $ [Ne III], and [N II] $\lambda 6585 := $ [N II], unless otherwise specified.

2. Methodology and Measurements

2.1. Grism Observations and Data Reduction

The BOSS 1244 protocluster was discovered via the MAMMOTH technique (Cai et al. 2016) and spectroscopically confirmed by LBT/MMT IR spectroscopy (Shi et al. 2021). The Grizli software package[8] is utilized in reducing the paired pre-imaging and grism exposures, following our previous work (Wang et al. 2022, hereafter W22). In brief, Grizli preprocesses the raw WFC3 exposures by flagging the pixels affected by cosmic rays and persistence, correcting for master and variable sky background caused by the metastable helium glow and performing WCS alignment to the Gaia DR2 astrometry frame. After preprocessing, Grizli constructs forward models of the full field-of-view (FoV) grism exposures at the visit level in an iterative manner. As a result, at the last iteration when the forward-modeling converges, Grizli produces a catalog of source redshift and extracted physical properties, e.g., emission-line fluxes and spectral indices. For all sources in this catalog, we also extracted their 1D/2D grism spectra and nebular emission-line 2D postage stamps, with a 60 mas plate

---

scale, Nyquist-sampling the WFC3 PSF. We use the same data products as in W22.

2.2. Sample Selection

The preselection of the sample has been discussed in detail in our previous work (W22). In brief, we fit linear combinations of spectral templates to the optimally extracted 1D grism spectra to infer the grism redshifts. We then compile a sample of 55 spectroscopically confirmed galaxies at $z \sim 2.24$, which are likely member galaxies of the BOSS 1244 protocluster (Shi et al. 2021). We also use 1D Gaussian profiles at corresponding wavelength centers to fit their intrinsic nebular emission lines and thus obtain emission-line fluxes ([O III], [O II], Hγ, Hβ, and Hδ). We then select sources with [O III] and [O II] emission lines with both lines having S/N $\geqslant 3$. From our diffraction-limited WFC3/G141 spectroscopy of these objects, we obtain their 2D emission-line maps, extracted from their 2D grism spectra after removing their best-fit 2D models of source stellar continua. We follow the custom technique developed by Wang et al. (2020) to deblend the self-contaminating line complex of the Hβ + [O III]$\lambda\lambda 4960,5008$ doublets to produce 2D maps of [O III]$\lambda 5008$ and Hβ clean of the orientation-specific contamination of [O III]$\lambda 4960$.

We also considered active galactic nucleus (AGN) ionization because the strong-line calibrations used to infer metallicity are not valid for the AGN ionization. We rely on the mass-excitation diagram (Juneau et al. 2014; Coil et al. 2015) to exclude AGN candidates in our sample. We identified three galaxies as being likely AGNs (see the right panel of Figure 3 in W22).

To securely measure metallicity gradients, we apply Voronoi tessellation (Cappellari & Copin 2003) to each galaxy's [O III] map to bin it into subregions, each having S/N > 2.5 in [O III]. We further select sources having more than 10 Voronoi bins in order to have enough points to fit metallicity gradients reliably. Finally, we have 20 galaxies that passed our selection criteria and 1 galaxy satisfying all criteria except AGN contamination. We keep the AGN data point in Figures 2 and 3 but omit it in other analyses. The integrated metallicity of this AGN is inferred from 2D line-flux maps with the center masked out by a projected $r = 1.5$ kpc disk to exclude regions contaminated by the central AGN.

2.3. Radial Metallicity Gradients

Following previous analyses, we assume that all galaxies in our sample are thin rotating disks, supported by recent spatially resolved observations of the ionized gas radial velocity fields at similar redshifts with $M_* \gtrsim 10^9 M_\odot$ (see, e.g., Jones et al. 2010; Förster Schreiber et al. 2018). The apparent elliptical morphology of galaxies stems from their inclination. Once we fit the inclination angle, we can deproject the images to the source plane and therefore get the intrinsic galactocentric distance. We use the software GALFIT (Peng et al. 2002) to fit each source morphology. We fit 2D Sérsic profiles convolved with the PSF to the direct F160w image. The free parameters in the fitting are the xy coordinates of the galaxy center, the major-axis effective radius R_e, the Sérsic index n, the projected axis ratio b/a, and the position angle (PA). We use the σ image internally generated by GALFIT in the fitting. For galaxies with irregular shapes (e.g., ID 1435), we use multiple Sérsic components in the fitting, and we use the measurements from the brightest

---

component. We get the inclination angle i through the simple relation: $\cos(i) = b/a$. The fitted results for our 20 galaxies are listed in Table 1.

We follow procedures in W22 to jointly constrain metallicity $(12 + \log(O/H))$, nebular dust extinction (A_v), and dereddened $H\beta$ flux $(f_{H\beta})$ using our forward-modeling Bayesian inference method. The likelihood function is defined as

$$L \propto \exp\left(-\frac{1}{2} \cdot \sum_i \frac{(f_{EL_i} - R_i \cdot f_{H\beta})^2}{(\sigma_{EL_i})^2 + (f_{H\beta})^2 \cdot (\sigma_{R_i})^2}\right), \qquad (1)$$

where f_{EL_i} and σ_{EL_i} represent the dereddened emission-line (e.g., [O II], $H\gamma$, $H\beta$, [O III]) flux[9] and its uncertainty, corrected using the Calzetti et al. (2000) dust extinction law with A_v as a free parameter. The emission-line maps are smoothed by an $FWHM = 0''.2$ Gaussian kernel, corresponding to the spatial resolution of HST. R_i corresponds to the expected line-flux ratios between EL_i and $H\beta$ (i.e., R_i can be the Balmer decrement of $H\gamma/H\beta = 0.47$ and the metallicity diagnostics of [O III]/$H\beta$ and [O II]/$H\beta$) and σ_{R_i} is their intrinsic scatter. The EMCEE package is employed to perform the Markov Chain Monte Carlo sampling.

The metallicity measurements are dependent on the specific calibration we choose because R_i and σ_{R_i} are given by strong-line calibrations. See W22 for a detailed discussion of the different choices. Here we adopt the empirical strong-line calibration in Bian et al. (2018) to convert emission-line-flux ratios to metallicity.

We apply the metallicity inferred above to each Voronoi bin in galaxies in our sample, so that we can investigate the relation between metallicity and the galactocentric distance. The Voronoi tessellation (as used in W20) is superior to averaging the signal in radial annuli (as is used in F18) because of azimuthal variations in chemical abundance discovered in nearby spiral galaxies (Ho et al. 2017). We use a simple linear least-squares method to fit the metallicity gradients with the following formula:

$$12 + \log(O/H) = \theta_0 + \theta_1 r \qquad (2)$$

Here θ_0 and θ_1 are the intercept and the gradient of the linear function, respectively, and r is the deprojected galactocentric radius in kiloparsec.

3. Results

3.1. Galaxies' Morphology

We run Galfit as discussed in Section 2 and list the results in Table 1. We notice that most of our galaxies have a regular morphology, i.e., they can be well fitted by a single Sérsic profile. The exceptions are ID 00313 and ID 01435. They show patterns of off-center clumps. Those may be attributed to star-forming clumps formed by gravitational instabilities in turbulent gas-rich disks (Zanella et al. 2015). Considering that the $\chi^2 = 1.88$ for ID 00313 fitted by Galfit is still acceptable, we retain this result. Because the clump in ID 01435 is more prominent, we therefore add multiple components for this galaxy and use the brightest component to derive the galaxies' morphology properties.

---

[9] When computing the integrated metallicity, the flux is calculated by fitting multiple Gaussian profiles to the extracted 1D spectra (see Section 3.4 in W22 for details) instead of using 2D emission maps such as when calculating metallicity gradients.

3.2. Mass Dependence of Metallicity Gradients

We list the metallicity gradient measurements in Table 1. An example of the fitting together with the galaxy's emission-line maps is shown in Figure 1, and the entire sample is shown in Figure 6 in the Appendix. At the 1σ confidence level, 2 and 1 galaxies have inverted and negative gradients (i.e., positive or negative and 1σ away from being flat), while 17 of the 20 galaxies are consistent with flat gradients. It is surprising that most of our galaxies have flat or marginally inverted gradients, lacking negative gradients, in contrast to expectations from previous cosmological hydrodynamic simulations and observations in blank fields at similar redshifts.

In Figure 2, we show the metallicity gradients as a function of the stellar mass, compared with previous observations in blank fields with sub-kpc resolution and simulations at a similar redshift of $z \sim 2$. W17 and W20 collect a galaxy sample with a stellar-mass range of $[10^7, 10^{10}]M_\odot$ using HST WFC3 NIR grisms through the Grism Lens-Amplified Survey from Space (GLASS) program; F18 measured galaxies in the mass range of $[10^8, 10^{11}]M_\odot$ using SINFONI at VLT assisted with adaptive optics. These two samples have robust measurements on radial gradients due to their sub-kpc resolution. There also exist other observations at high redshift (Stott et al. 2014; Wuyts et al. 2016; Curti et al. 2020) yet these data are taken under natural seeing. In simulations, Ma et al. (2017) studied a galaxy sample in the mass range $[10^8, 10^{11}]M_\odot$ from Feedback in Realistic Environments (FIRE) simulations implementing the strong feedback scheme; Hemler et al. (2021) have a galaxy sample in the mass range $[10^9, 10^{11}]M_\odot$ from the TNG50 star-forming galaxy population. The predictions of FIRE simulations match well with the negative gradients in F18. And there are also predominantly negative gradients in the TNG50 simulation. However, our sample shows a large fraction of flat/inverted gradients, where the weighted average metallicity gradient in the BOSS 1244 field is 0.010 ± 0.005; this is hardly seen in F18, where the weighted average metallicity gradient is -0.041 ± 0.004. The inverted gradients are also found in W20, while our samples have a wider stellar-mass range in $\log(M_*/M_\odot) = [9.5, 10.5]$, which strongly suggests that inverted gradients also exist in galaxies with higher masses.

3.3. Environmental Effects

We plot metallicity gradients as a function of the integrated galaxy metallicity on the left panel of Figure 3. We see evidence for an anticorrelation between the metallicity and metallicity gradient (hereafter the Zgrad-Z relation for simplicity), with Pearson coefficient $r = -0.49$ and p-value $p = 0.03$. This low p-value indicates that the metallicity and metallicity gradients are correlated at the 95% confidence level. We find that metal-rich galaxies tend to show negative metallicity gradients, while metal-poor galaxies are more likely to have inverted gradients. It is also consistent with the galaxy mass dependence of the metallicity gradient, in the sense that more massive galaxies tend to be more metal rich (Salim et al. 2015) and the metallicity gradient is anticorrelated with mass (Ma et al. 2017; Wang et al. 2020).

When primordial gas flows into a galaxy, it dilutes the central metal abundance, raises the metallicity gradient, and, at the same time, also dilutes the integrated metallicity of the galaxy. This can explain why we tend to see stronger inverted metallicity gradients for metal-poor galaxies. In Figure 4, we

Table 1
Derived Physical and Morphological Properties of the Galaxies

ID	R.A. (deg.)	Decl. (deg.)	z_{grism}	δ_g	Photometry (ABmag)					Morphology Properties				Derived Physical Properties			
					F125W	F160W	U	z	K_s	R_e	b/a	PA	χ^2	$\log(M_*/M_\odot)$	SFR $(M_\odot\ yr^{-1})$[a]	$12 + \log(O/H)$	∇Z (dex kpc^{-1})
00262[b]	190.938355	35.849177	2.22	16.38	22.59	21.83	24.71	23.04	20.50	1.95	0.75	16.95	1.33	$11.43^{+0.03}_{-0.04}$	$51.01^{+9.03}_{-8.51}$	$8.40^{+0.09}_{-0.11}$	0.050 ± 0.045
00313	190.902894	35.851659	2.23	18.57	24.45	23.68	25.50	24.21	22.61	2.63	0.29	17.07	1.88	$10.31^{+0.06}_{-0.08}$	$10.64^{+1.27}_{-1.52}$	$8.35^{+0.08}_{-0.08}$	0.003 ± 0.021
00613	190.921119	35.865813	2.24	20.68	24.30	23.78	25.38	24.37	22.82	2.24	0.44	40.15	1.20	$10.18^{+0.07}_{-0.10}$	$9.32^{+1.01}_{-1.03}$	$8.41^{+0.10}_{-0.12}$	0.006 ± 0.048
00769	190.909740	35.871348	2.24	22.21	23.43	23.05	24.43	23.35	22.25	2.36	0.71	−14.18	1.39	$10.12^{+0.11}_{-0.15}$	$23.06^{+4.72}_{-4.33}$	$8.37^{+0.08}_{-0.08}$	0.036 ± 0.043
00996	190.873758	35.880726	2.32	22.47	23.96	23.41	25.86	24.12	23.04	1.14	0.50	−63.54	1.22	$10.10^{+0.09}_{-0.11}$	$38.61^{+10.12}_{-6.78}$	$8.30^{+0.13}_{-0.14}$	0.012 ± 0.066
01335	190.871757	35.895697	2.24	24.14	23.04	22.72	24.41	22.81	21.73	4.11	0.43	86.05	1.34	$10.13^{+0.09}_{-0.09}$	$114.05^{+22.49}_{-29.10}$	$8.56^{+0.07}_{-0.08}$	-0.041 ± 0.040
01394	190.877806	35.898194	2.21	24.99	23.81	23.61	24.84	23.67	22.71	0.99	0.40	24.13	1.31	$9.31^{+0.11}_{-0.08}$	$24.75^{+4.79}_{-4.45}$	$8.51^{+0.06}_{-0.07}$	0.014 ± 0.035
01435	190.869813	35.900036	2.21	24.33	23.46	23.13	25.35	23.24	22.27	1.02	0.97	−5.47	1.25	$9.89^{+0.09}_{-0.07}$	$93.26^{+15.22}_{-12.83}$	$8.35^{+0.08}_{-0.09}$	0.025 ± 0.048
01464	190.873403	35.901270	2.21	24.84	23.81	23.40	25.83	24.01	22.49	1.31	0.43	74.13	1.34	$10.08^{+0.11}_{-0.12}$	$33.40^{+6.59}_{-5.93}$	$8.49^{+0.07}_{-0.08}$	-0.012 ± 0.042
01467	190.869254	35.901455	2.21	24.39	24.00	23.51	25.52	23.88	23.43	1.68	0.40	−71.41	1.40	$9.80^{+0.08}_{-0.08}$	$34.16^{+9.66}_{-6.89}$	$8.24^{+0.10}_{-0.10}$	0.037 ± 0.027
01890	190.865939	35.913638	2.25	24.77	25.08	24.36	26.36	24.43	24.36	1.93	0.46	17.43	1.17	$9.14^{+0.07}_{-0.06}$	$17.05^{+2.71}_{-2.40}$	$8.28^{+0.11}_{-0.12}$	0.057 ± 0.074
01998	190.868202	35.916375	2.21	25.16	22.83	22.49	23.94	22.26	21.25	1.89	0.95	−37.99	1.55	$10.30^{+0.08}_{-0.09}$	$121.59^{+37.28}_{-26.68}$	$8.37^{+0.10}_{-0.11}$	0.003 ± 0.044
02327	190.927963	35.926164	2.24	23.65	23.99	23.52	25.93	24.25	22.82	1.08	0.65	57.80	1.22	$10.01^{+0.13}_{-0.15}$	$24.76^{+4.96}_{-4.73}$	$8.39^{+0.08}_{-0.08}$	0.014 ± 0.053
02330	190.905581	35.926178	2.29	25.99	22.78	22.39	25.42	22.89	21.27	1.31	0.97	23.60	1.29	$10.34^{+0.07}_{-0.07}$	$238.14^{+24.23}_{-24.36}$	$8.43^{+0.07}_{-0.08}$	0.038 ± 0.037
02992	190.843993	35.949979	2.35	21.76	23.84	23.29	26.40	23.67	22.97	1.37	0.72	−86.93	1.30	$9.95^{+0.08}_{-0.06}$	$109.41^{+17.00}_{-15.95}$	$8.49^{+0.08}_{-0.10}$	-0.061 ± 0.085
03061	190.838668	35.953087	2.23	20.82	23.07	22.73	24.39	22.90	21.82	2.79	0.36	−36.25	1.25	$10.15^{+0.10}_{-0.10}$	$49.78^{+9.25}_{-8.66}$	$8.41^{+0.07}_{-0.07}$	-0.008 ± 0.022
03155	190.842877	35.957764	2.32	21.37	23.48	23.02	26.32	23.60	22.00	2.44	0.80	58.41	1.30	$10.27^{+0.09}_{-0.08}$	$207.88^{+30.67}_{-28.99}$	$8.55^{+0.08}_{-0.10}$	0.041 ± 0.058
03276	190.857451	35.964185	2.21	22.77	22.48	22.18	24.04	22.20	21.43	3.13	0.54	−9.10	1.51	$10.22^{+0.10}_{-0.07}$	$189.85^{+30.04}_{-25.10}$	$8.39^{+0.06}_{-0.06}$	0.012 ± 0.021
03331	190.862922	35.967686	2.22	22.89	24.04	23.71	25.20	23.71	22.76	1.78	0.34	−6.72	1.23	$9.40^{+0.12}_{-0.10}$	$28.11^{+4.40}_{-5.40}$	$8.29^{+0.10}_{-0.11}$	0.017 ± 0.052
03495	190.853920	35.977367	2.23	21.48	23.72	23.22	26.49	23.70	22.86	1.62	0.59	−53.70	1.22	$10.00^{+0.09}_{-0.06}$	$123.79^{+21.15}_{-17.29}$	$8.40^{+0.07}_{-0.07}$	0.023 ± 0.044
03516	190.851775	35.979114	2.23	21.17	23.79	23.46	25.86	23.63	22.71	2.50	0.45	−27.16	1.20	$9.80^{+0.10}_{-0.06}$	$75.17^{+13.24}_{-9.98}$	$8.44^{+0.10}_{-0.11}$	0.022 ± 0.047

Notes.

[a] The SFR is derived through SED fitting using J- (HST F125W), H- (HST F160W), U- (LBT/LBC Uspec), z- (LBT/LBC z-SLOAN), and K_s-band (CFHT K_s) photometry, assuming a constant star formation history, but the SFR in our previous work (W22) is derived through dust-corrected Hβ flux.

[b] This object is classified as an AGN. Its integrated metallicity is inferred from 2D line-flux maps with the center masked out by a deprojected $r = 1.5$ kpc disk to discard regions contaminated by the central AGN, whereas the line fluxes for objects without AGNs are estimated from fitting 1D Gaussian profiles in 1D spectra.
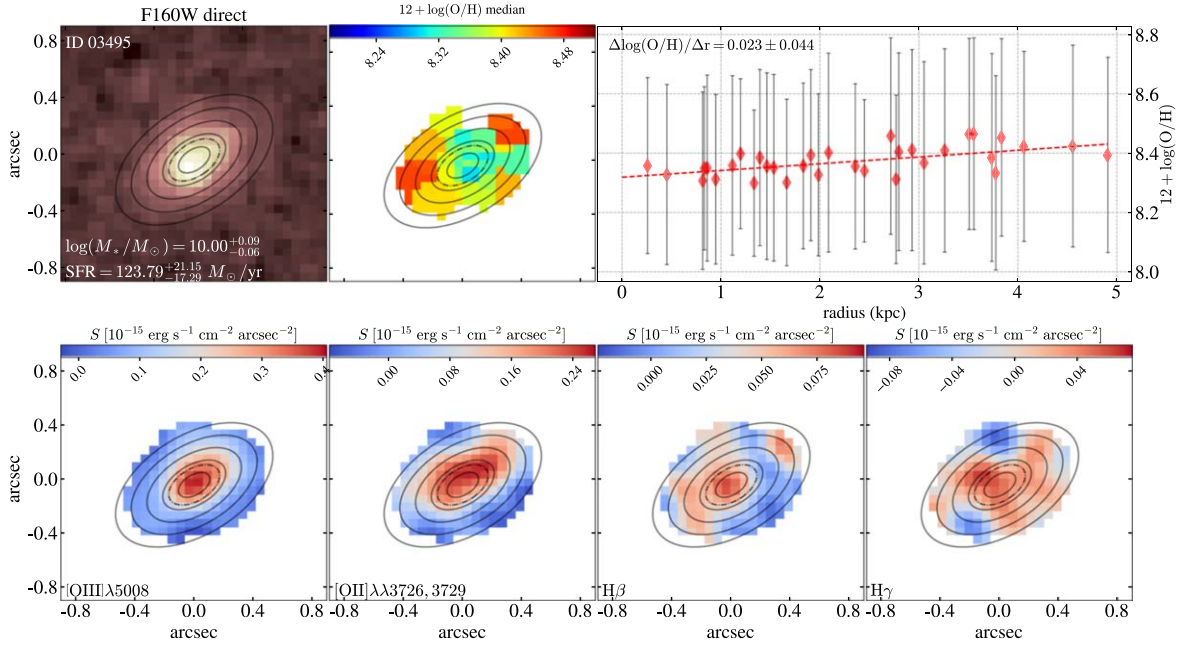
Figure 1. The galaxy ID 03495 as an example of the analysis procedures applied to our entire sample. Top, from left to right: the F160W image of this galaxy, its metallicity map, and radial gradient. The black solid contours mark the deprojected galactocentric radii with a 1 kpc interval. The black dashed–dotted ellipses mark the half-light radii fitted by Galfit. Bottom: The smoothed 2D emission-line maps ([O III], [O II], Hβ, and Hγ) are used to infer the metallicity map. In all maps, north is up and east is to the left.
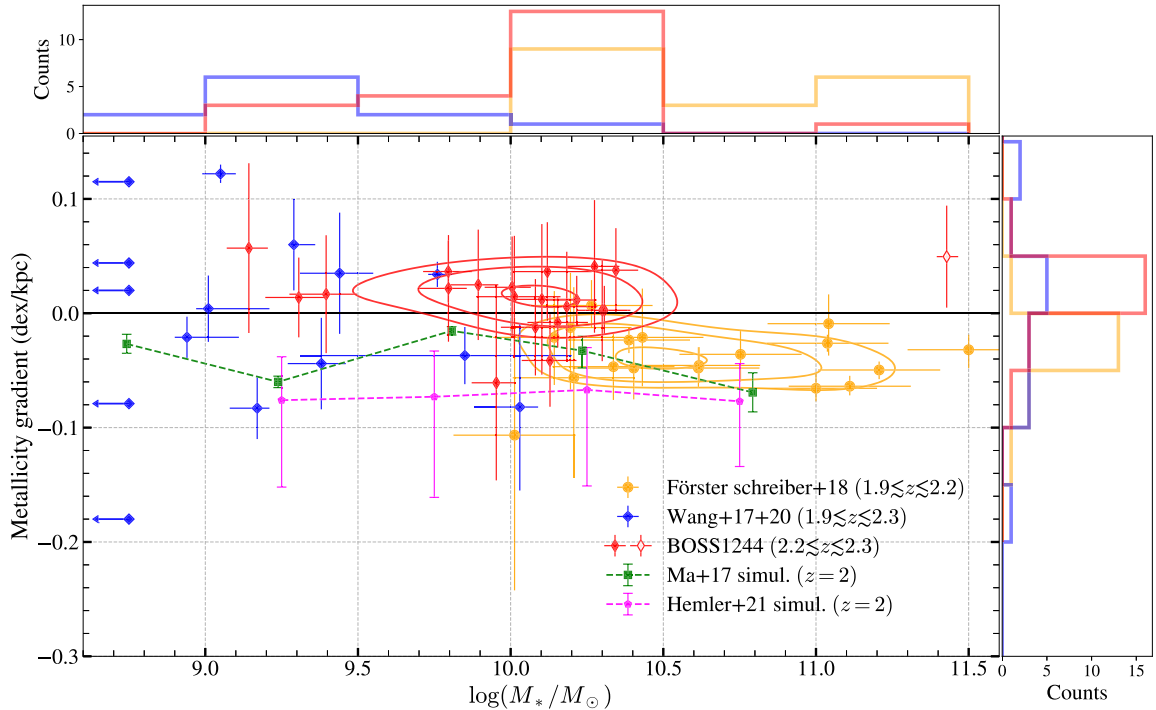

Figure 2. The metallicity gradients as a function of stellar mass for high-z star-forming galaxies in blank fields and overdense environments. The red diamonds are from our BOSS 1244 field, and the hollow one marks the galaxy categorized as an AGN. The orange circles are observed in F18. The blue diamonds come from the combined sample in W17 and W20, and the ones with left-pointing arrows represent dwarf galaxies ($\log(M_*/M_\odot) < 8.5$). These upper limits are omitted from our comparison for being far from our sample mass range. The red and orange contours denote the 50th, 68th, and 95th percentiles of the distribution estimated with Gaussian KDE. The dashed green line is the population stack of five mass bins from FIRE simulations (Ma et al. 2017). The magenta dashed line is the population stack of four mass bins from TNG50 simulations (Hemler et al. 2021). The histograms on the top and right of the main figure show the number distribution of observed stellar masses and metallicity gradients, respectively. From the histogram, our sample has the largest number of galaxies in the mass range $\log(M_*/M_\odot) = [10, 10.5]$ and has a notable number and fraction of inverted metallicity gradients.

show the mass–metallicity relation (MZR) of our 20 galaxies residing in extreme overdensities and that from the MOSDEF survey targeting blank fields, at similar redshifts ($z \sim 2.3$) (Sanders et al. 2021). The comparison of the MZRs in our BOSS 1244 high-density field and the MOSDEF blank fields has already been discussed in W22, and here we only focus on
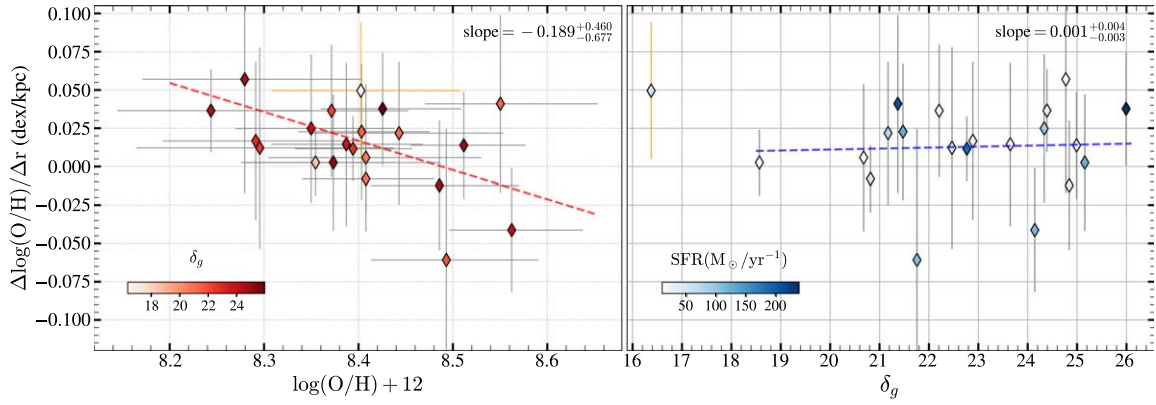
Figure 3. Left: relation between metallicity gradients and global metallicity of our galaxies. The red dashed lines show the linear fitting of the data using the LINMIX software with the 1σ error of both metallicity and metallicity gradient taken into account. The data points are color-coded by their environment overdensity δ_g. The diamond with an orange error bar marks the galaxy classified as an AGN, which is excluded in the linear fitting in both left and right panels. Right: the metallicity gradients as a function of overdensity δ_g of our samples. The data points are color-coded in SFR. The blue dashed line is also the linear fitting using LINMIX, taking into account the 1σ errors of the metallicity gradients. The data points are color-coded in SFR.
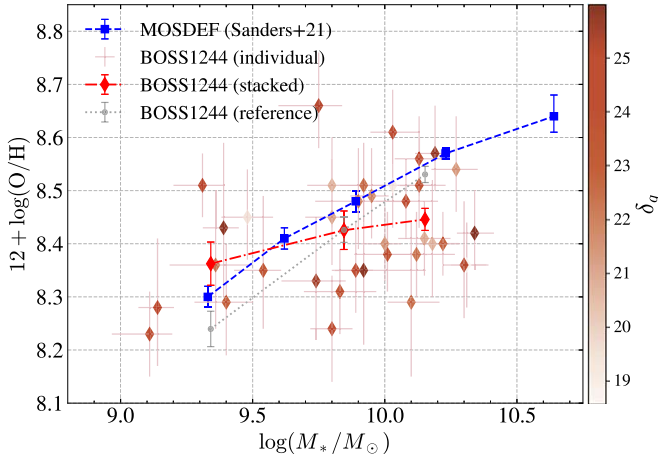
Figure 4. The mass–metallicity relation (MZR) for our galaxy sample compared with the MZR measured in the field by the MOSDEF survey at $z \sim 2.3$ (Sanders et al. 2021). The diamonds with pink bars represent individual galaxies, color-coded in overdensity δ_g. The red and blue lines correspond to the stacks of galaxies in our BOSS 1244 protocluster and the MOSDEF fields. The gray dotted line shows the reference MZR derived using the Sanders et al. (2021) FMR assuming the SFR and M_* of our sample galaxies. We see that our galaxies residing in overdense environments show significant metallicity deficiency, compared with their coeval field counterparts, particularly in the high-mass regime. Here we not only show the 20 galaxies in this work, but also the other 16 galaxies in W22, to illustrate the relation in our protocluster environment with stronger statistical significance.

galaxies with metallicity gradient measurements. We caution that these surveys have different line-flux limits, which results in different source selections that can affect the behavior of the MZR (see a recent comprehensive analysis by Henry et al. 2021). To account for this selection effect, we employ the fundamental metallicity relation (FMR) prescribed by Sanders et al. (2021) to derive the field reference values of metallicities for our galaxies.

We find a marked deficiency of metallicity for our galaxies, in particular with $M_* \sim 10^{10} M_\odot$, as compared to their field reference values. This metallicity deficiency is possibly caused by the combined effects of cold-mode gas accretion from cosmic filaments (Kereš et al. 2009) and metal-enriched gas removal by ejective feedback (Muratov et al. 2015). Kleiner et al. (2017) found that massive galaxies, with their deep gravitational potentials, should accrete cold IGM gas from the

intrafilament medium. We suggest that the gravitational potential of the cluster-scale dark matter halo in overdense environments would also draw primordial gas from the IGM through cosmic filaments. This cold-mode accretion boosted by the extremely massive protocluster dominates our high-mass galaxies, diluting the metallicity, making them more metal-poor than their coeval field counterparts. The star-forming feedback blows metal-rich winds outward and flattens/inverts the metallicity gradients (Wang et al. 2019). For energy-driven winds, the mass loading factor is $\eta \propto v_{vir}^{-2} \propto M_h^{-1/3}$, and $\eta \propto v_{vir}^{-1} \propto M_h^{-2/3}$ for momentum-driven winds. Thus, the fraction of metal-rich gas that is blown outward by feedback decreases with halo mass, so the outflows are suppressed in high-mass galaxies due to their massive DM halos, as well as the cluster-scale DM halo. In this case, the cold-mode accretion enhanced by the protocluster environment should dominate for most of the galaxies, while star formation feedback that is suppressed by DM halos would play a minor role.

On the right panel of Figure 3, we plot the relation between metallicity gradient and galaxy overdensity δ_g, where δ_g is defined as $\delta_g = \frac{\Sigma_{group}}{\Sigma_{group}} - 1$, Σ_{group} is the Hα emitter (HAE) number per arcmin^2 within the overdensity, and Σ_{field} is the surface density of HAEs in random fields. We estimate the δ_g field by fitting 2D kernel density estimation (KDE) to the HAE map with a $200''$ ($\sim 5.3c$ Mpc) Gaussian kernel, normalized by the maximum δ_g of the group calculated in Shi et al. (2021). We also use LINMIX to fit a linear relation. We find no significant correlation between metallicity gradient and δ_g, with a Pearson coefficient $r = 0.17$ and p-value $p = 0.46$. The protocluster may be too dense to reach a certain threshold (all sample galaxies reside in a similarly overdense environment, far denser than blank fields), at which there is enough gas to replenish all the member galaxies; thus, the metallicity mainly depends on each galaxy's individual properties. Thus, the trend that metallicity gradients grow as overdensity increases is not so obvious. We expect a more significant correlation as the galaxy sample continues to accumulate in the MAMMOTH-Grism survey.

4. Conclusion

We have presented the first sample of gas-phase metallicity radial gradients measured in overdense environments at $z > 2$

using grism slitless spectroscopy. The data presented in this work were acquired by MAMMOTH-Grism in the HST cycle 28 medium program. The BOSS 1244 protocluster field is among three of the most massive galaxy protoclusters at $z \sim 2.2$–2.3 identified using the MAMMOTH technique, in which we selected a sample of 20 protocluster member galaxies with $M_*/M_\odot \in [10^9, 10^{10.3}]$, $SFR \in [10, 240]M_\odot \, yr^{-1}$, and $12 + \log(O/H) \in [8.2, 8.6]$ to measure metallicity gradients. We find an unprecedentedly large fraction of flat/inverted gradients in this protocluster environment, compared with that of MOSDEF field galaxies. At the 1σ confidence level, we find 2/20 of galaxies showing inverted gradients and 17/20 with no significant gradients. This differs from the usual trend of negative gradients. We find an anticorrelation between metallicity gradients and integrated metallicity. We conclude that these notable flat/inverted gradients are likely caused by strong cold-mode accretion in protoclusters. The overdense environments boost cold-mode accretion by dragging more primordial gas through cosmic filaments and injecting it into the galaxies' centers through the strong gravitation of the massive cluster-scale DM halo. The primordial gas directly dilutes the integrated metallicity and also flattens/inverts the metallicity gradients. This scenario is consistent with the anticorrelation between metallicity gradients and integrated metallicity, where we expect the galaxy to be more metal poor when it shows a higher metallicity gradient in response to gas diluting its center.

While the hydrodynamical simulations so far match the negative metallicity gradients well for field galaxies, they cannot reproduce our findings in overdense environments. This also suggests that future hydrodynamical simulations should take such environmental effects into consideration to investigate the galaxy mass assembly processes in protoclusters.

The ongoing MAMMOTH-Grism program includes two other protocluster fields, BOSS 1542 and BOSS 1441 (Cai et al. 2017; Shi et al. 2021). We expect our statistics will be improved once all the data are acquired by HST and analyzed, when the sample size will be three times as large as now. This MAMMOTH-Grism full sample of galaxies at cosmic noon in

extremely overdense environments provides a unique opportunity for us to further understand environmental effects on galaxy formation.

Software: EMCEE (Foreman-Mackey et al. 2013), Grizli (Brammer & Matharu 2021), GALFIT (Peng et al. 2002), VorBin (Cappellari & Copin 2003), LINMIX (Kelly 2007).

Appendix A
Systematic Error Estimation Using Mocks

To test the robustness of our method and estimate the systematic error, we use mocks to compare the reconstructed metallicity gradients with the input values. To build a simplified model of emission-line maps, we consider a face-on galaxy with Hβ having a Sérsic profile with index $n = 0.5$ and $R_e = 1.5$ kpc. We then assign the metallicity to the disk with given gradients and obtain other line maps ([O III], [O II], and Hγ) from the Hβ maps considering the metallicity calibrations in Bian et al. (2018). We add Gaussian random noise to the line maps so that they have the desired S/N. We then apply the pipeline discussed in our paper to the mock emission-line maps to calculate the metallicity gradients. In the mocks, we choose five metallicity gradients: [0, 0.02, 0.04, -0.02, -0.04] dex kpc^{-1}, and $(S/N)_{H\beta} = 3$, comparable to the median $(S/N)_{H\beta} = 3.4$ of our sample galaxies.

We run each case 100 times and estimated the systematic error to be ~ 0.02 dex kpc^{-1}. From the first panel of Figure 5, we find that the reconstructed metallicity gradients generally agree with the true values within 1σ in all five cases. We also note that the reconstructed gradients tend to be flat: The reconstructed gradients are less steep than the original input
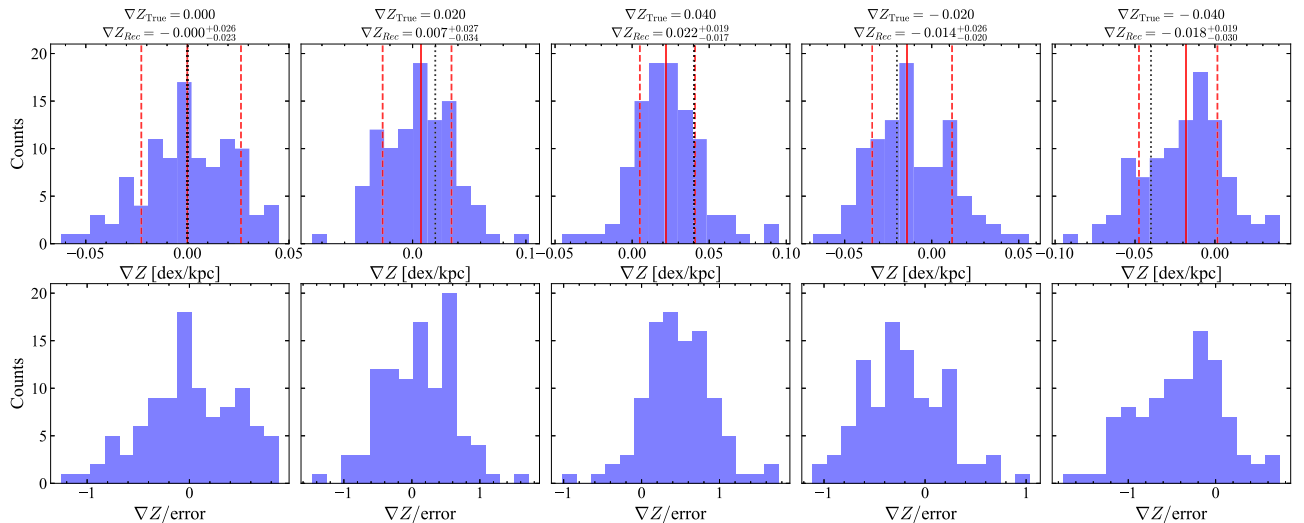
Figure 5. The histogram of the fitted metallicity gradients (top), and the metallicity gradients divided by their uncertainties (bottom). From left to right: the results for five different mocks with true gradients [0, 0.02, 0.04, -0.02, -0.04] dex kpc^{-1}. The black dotted line denotes the true gradient value. The solid red line represents the median value in the 100 reconstructions, and the red dashed lines show the 1σ interval.
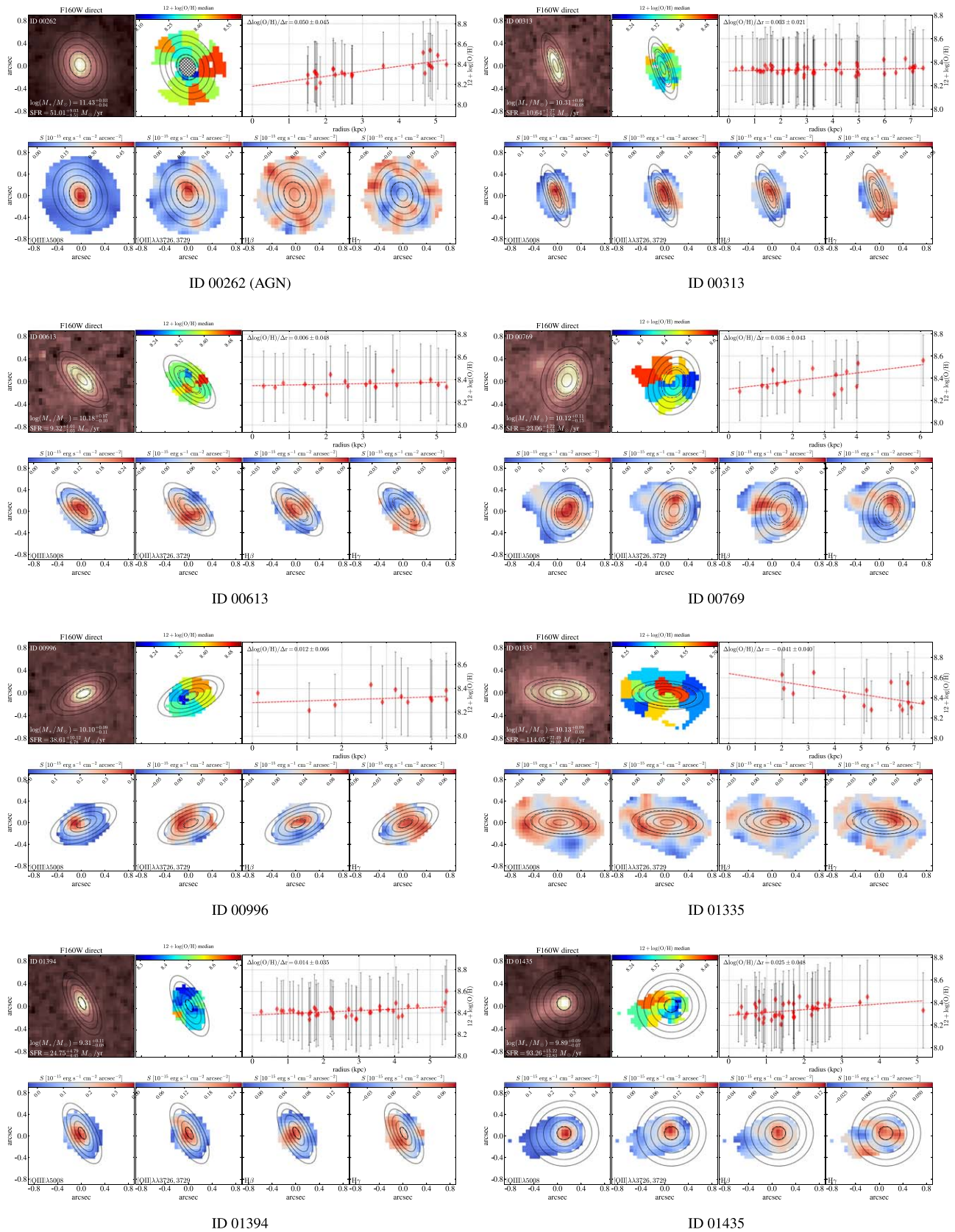
ID 00262 (AGN)

ID 00313

ID 00613

ID 00769

ID 00996

ID 01335

ID 01394

ID 01435

Figure 6. Metallicity radial gradients measured in our sample. The same as Figure 1.

ID 01467

ID 01464

ID 01890

ID 01998

ID 02330

ID 02327

ID 02992

ID 03061
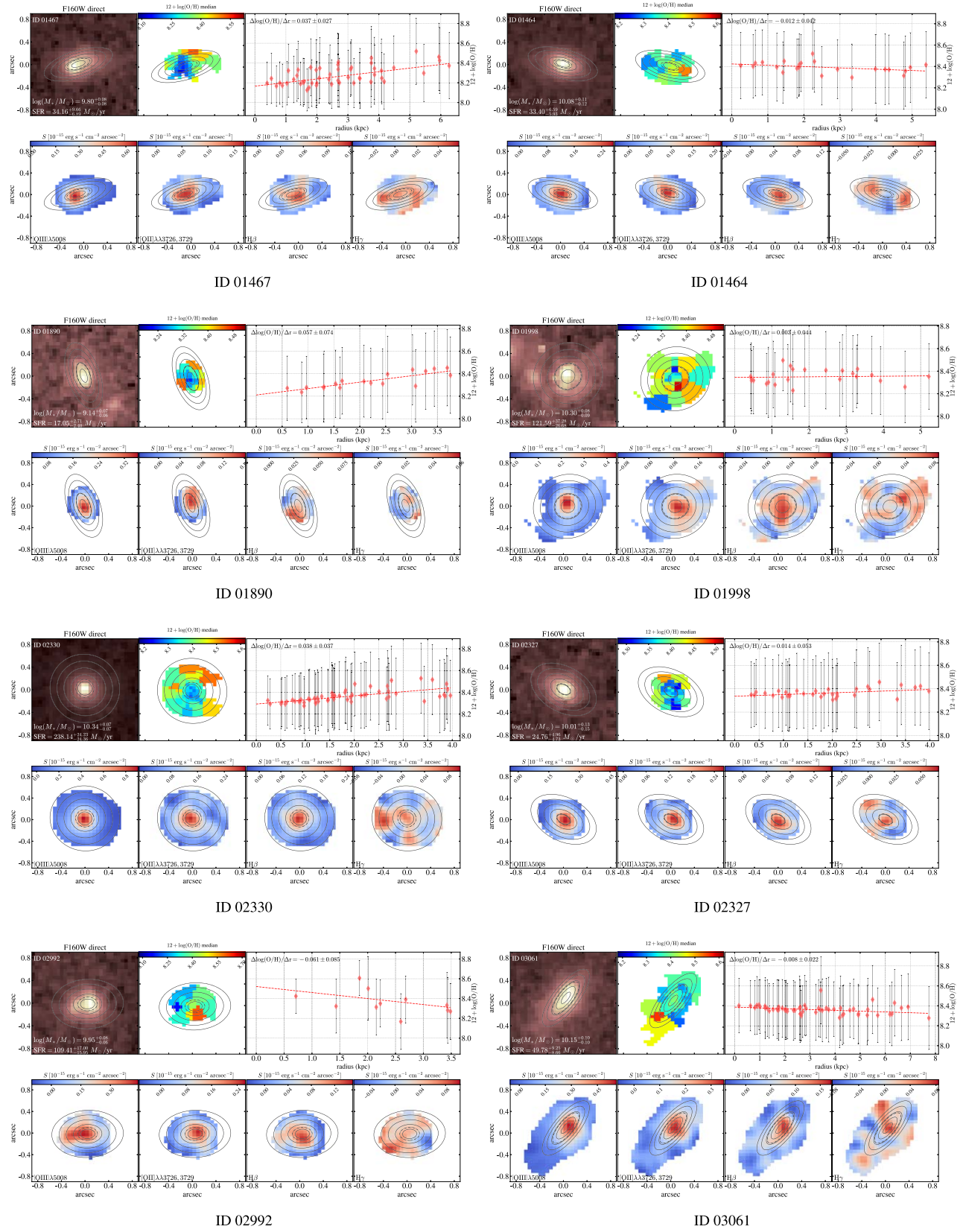
Figure 6. (Continued.)

ID 03155
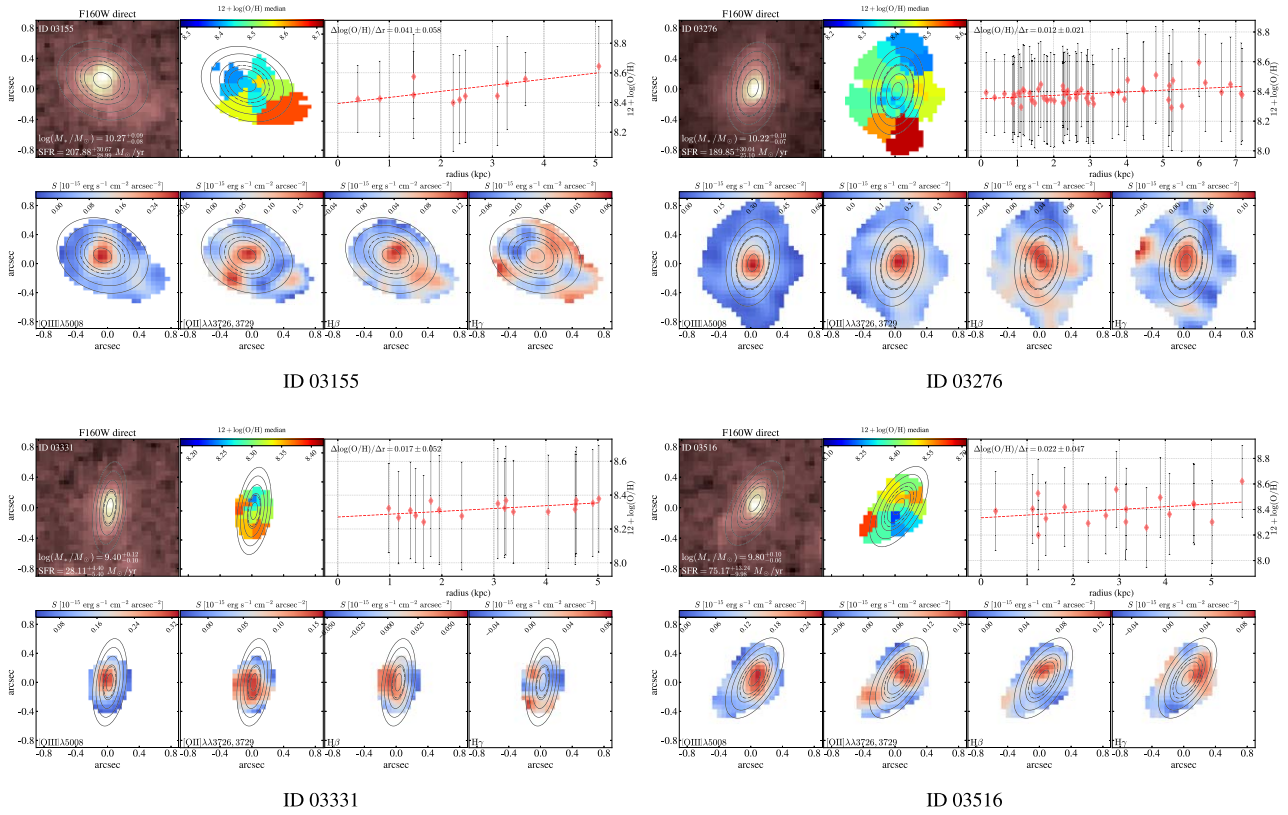

ID 03276

ID 03331

ID 03516

Figure 6. (Continued.)

values for both positive and negative cases. From the second panel, we find that most of the measurements are below the 1σ significance level, similar to the situation of our measurements in the BOSS 1244 field.

Interestingly, in the two mocks with positive gradients, we find that the ratio of positive reconstructed gradients is [59%, 87%] for $\nabla Z_{\mathrm{True}} = [0.02, 0.04]$ dex kpc^{-1} respectively, while in our galaxy sample, the ratio of positive gradients is $16/20 = 80\%$. This hints that our sample galaxies tend to have intrinsic positive gradients, despite the relatively large uncertainty in metallicity calculation and gradient fitting.

Appendix B
Detailed Figures for Measuring Radial Gradients

In Figure 6, we show the gradients measurement as well as emission line maps of all the galaxies in our sample.

ORCID iDs

Zihao Li https://orcid.org/0000-0001-5951-459X
Xin Wang https://orcid.org/0000-0002-9373-3865
Zheng Cai https://orcid.org/0000-0001-8467-6478
Dong Dong Shi https://orcid.org/0000-0002-4314-5686
Xiaohui Fan https://orcid.org/0000-0003-3310-0131
Xian Zhong Zheng https://orcid.org/0000-0003-3728-9912
Matthew A. Malkan https://orcid.org/0000-0001-6919-1237
Harry I. Teplitz https://orcid.org/0000-0002-7064-5424
Alaina L. Henry https://orcid.org/0000-0002-6586-4446
Fuyan Bian https://orcid.org/0000-0002-1620-0897
James Colbert https://orcid.org/0000-0001-6482-3020

References

Bian, F., Kewley, L. J., & Dopita, M. A. 2018, ApJ, 859, 175
Brammer, G., & Matharu, J. 2021, gbrammer/grizli: Release 2021, 1.3.2, Zenodo, doi:10.5281/zenodo.5012699
Cai, Z., Fan, X., Bian, F., et al. 2017, ApJ, 839, 131
Cai, Z., Fan, X., Peirani, S., et al. 2016, ApJ, 833, 135
Calzetti, D., Armus, L., Bohlin, R. C., et al. 2000, ApJ, 533, 682
Cappellari, M., & Copin, Y. 2003, MNRAS, 342, 345
Carton, D., Brinchmann, J., Contini, T., et al. 2018, MNRAS, 478, 4293
Coil, A. L., Aird, J., Reddy, N., et al. 2015, ApJ, 801, 35
Cresci, G., Mannucci, F., Maiolino, R., et al. 2010, Natur, 467, 811
Curti, M., Maiolino, R., Cirasuolo, M., et al. 2020, MNRAS, 492, 821
Dekel, A., & Birnboim, Y. 2006, MNRAS, 368, 2
Dekel, A., Birnboim, Y., Engel, G., et al. 2009, Natur, 457, 451
Finlator, K., & Davé, R. 2008, MNRAS, 385, 2181
Foreman-Mackey, D., Hogg, D. W., Lang, D., & Goodman, J. 2013, PASP, 125, 306
Förster Schreiber, N. M., Renzini, A., Mancini, C., et al. 2018, ApJS, 238, 21
Hemler, Z. S., Torrey, P., Qi, J., et al. 2021, MNRAS, 506, 3024
Henry, A. L., Rafelski, M. A., Sunnquist, B., et al. 2021, ApJ, 919, 143
Ho, I. T., Kudritzki, R.-P., Kewley, L. J., et al. 2015, MNRAS, 448, 2030
Ho, I. T., Seibert, M., Meidt, S. E., et al. 2017, ApJ, 846, 39
Hou, J. L., Prantzos, N., & Boissier, S. 2000, A&A, 362, 921
Jones, T., Ellis, R. S., Richard, J., & Jullo, E. 2013, ApJ, 765, 48
Jones, T. A., Swinbank, A. M., Ellis, R. S., Richard, J., & Stark, D. P. 2010, MNRAS, 404, 1247
Juneau, S., Bournaud, F., Charlot, S., et al. 2014, ApJ, 788, 88
Kelly, B. C. 2007, ApJ, 665, 1489
Kereš, D., Katz, N., Fardal, M., Davé, R., & Weinberg, D. H. 2009, MNRAS, 395, 160
Kereš, D., Katz, N., Weinberg, D. H., & Davé, R. 2005, MNRAS, 363, 2
Kleiner, D., Pimbblet, K. A., Jones, D. H., Koribalski, B. S., & Serra, P. 2017, MNRAS, 466, 4692
Leethochawalit, N., Jones, T. A., Ellis, R. S., et al. 2016, ApJ, 820, 84
Ma, X., Hopkins, P. F., Feldmann, R., et al. 2017, MNRAS, 466, 4780

Muratov, A. L., Kereš, D., Faucher-Giguère, C.-A., et al. 2015, MNRAS, 454, 2691
Pagel, B. E. J., & Edmunds, M. G. 1981, ARA&A, 19, 77
Peng, C. Y., Ho, L. C., Impey, C. D., & Rix, H.-W. 2002, AJ, 124, 266
Peng, Y.-J., & Maiolino, R. 2014, MNRAS, 443, 3643
Rupke, D. S. N., Kewley, L. J., & Barnes, J. E. 2010, ApJL, 710, L156
Salim, S., Lee, J. C., Davé, R., & Dickinson, M. 2015, ApJ, 808, 25
Sanders, R. L., Shapley, A. E., Jones, T., et al. 2021, ApJ, 914, 19
Searle, L. 1971, ApJ, 168, 327
Shi, D. D., Cai, Z., Fan, X., et al. 2021, ApJ, 915, 32
Simons, R. C., Papovich, C., Momcheva, I., et al. 2021, ApJ, 923, 203
Stott, J. P., Sobral, D., Swinbank, A. M., et al. 2014, MNRAS, 443, 2695
Swinbank, A. M., Sobral, D., Smail, I., et al. 2012, MNRAS, 426, 935
Tissera, P. B., Rosas-Guevara, Y., Bower, R. G., et al. 2019, MNRAS, 482, 2208
Wang, X., Jones, T. A., Treu, T., et al. 2017, ApJ, 837, 89
Wang, X., Jones, T. A., Treu, T., et al. 2019, ApJ, 882, 94
Wang, X., Jones, T. A., Treu, T., et al. 2020, ApJ, 900, 183
Wang, X., Li, Z., Cai, Z., et al. 2022, ApJ, 926, 70
Wuyts, E., Wisnioski, E., Fossati, M., et al. 2016, ApJ, 827, 74
Zanella, A., Daddi, E., Le Floc'h, E., et al. 2015, Natur, 521, 54